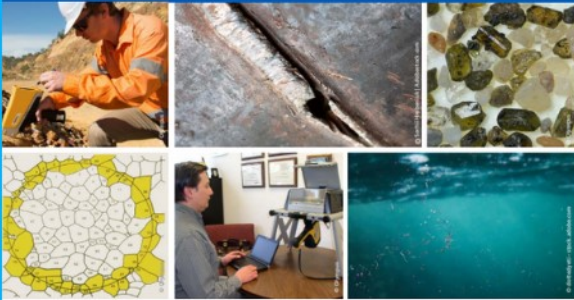




# 2<sup>nd</sup> Advanced Optical Metrology Compendium

## Advanced Optical Metrology

Geoscience | Corrosion | Particles | Additive Manufacturing: Metallurgy, Cut Analysis & Porosity



**EVIDENT**  
**OLYMPUS**

**WILEY**

The latest eBook from **Advanced Optical Metrology**.  
Download for free.

This compendium includes a collection of optical metrology papers, a repository of teaching materials, and instructions on how to publish scientific achievements.

With the aim of improving communication between fundamental research and industrial applications in the field of optical metrology we have collected and organized existing information and made it more accessible and useful for researchers and practitioners.

**EVIDENT**  
**OLYMPUS**

**WILEY**

# Nanoengineering Palladium Plasmonic Nanosheets Inside Polymer Nanospheres for Photothermal Therapy and Targeted Drug Delivery

Laura Uson, Cristina Yus, Gracia Mendoza, Eric Leroy, Silvia Irusta, Teresa Alejo, David García-Domingo, Ane Larrea, Manuel Arruebo,\* Raul Arenal, and Victor Sebastian\*

The incorporation of plasmonic nanoconstructs in biodegradable polymeric nanoparticles (NPs), together with therapeutic drugs in a controlled procedure is of interest for different applications in Nanomedicine. Advanced hybrid nanomaterials can be engineered by combining the in situ formation of plasmonic palladium nanosheets (NSs) and the proper ionic nature of the encapsulated drug. This study presents a new procedure to synthesize hybrid nanostructures by a Pickering double emulsion. Anisotropic palladium (Pd) NSs with unique near-infrared (NIR)-optical properties can be assembled within a poly lactic-co-glycolic acid matrix of < 200 nm NPs, when Pd precursors are in situ reduced via a gas-phase procedure. The hybrid nanomaterials respond to external NIR light stimulus. The unprecedented precision to assemble, in a single stage, plasmonic nanoconstructs having a total loading selectivity, when encapsulated in combination with hydrophobic drugs, offers new opportunities in the new class of theragnostics, in particular when triggered drug delivery and photothermal therapies are required.

and the toxicity and resistance associated to the drugs used, such as chemotherapy medicines, demand the design of more effective, safe, and reliable drug delivery vectors.<sup>[1]</sup>

Polymers are of interest in therapeutic applications because exhibit a great synthetic versatility to customize the targeted application and satisfy the stringent requirements of the regulatory authorities.<sup>[2]</sup> Polymers are engineered into the nanoscale<sup>[3]</sup> to circumvent some of the risks and disadvantages associated with traditional drug administration routes by controlling:<sup>[4]</sup> 1) the drug payload, 2) pharmacokinetics and release in the site of action, and 3) the internalization through biological membranes. Then, polymer nanoparticles (NPs) enable maintaining the therapeutic efficacy and the active targeting to the specific site needed of therapeutic action.


Polymer NPs can be designed to improve drug bioavailability (i.e., the portion of the bioactive compound that reaches systemic circulation and performs the therapeutic functions), by: 1) increasing drug absorption through enhanced solubility, this is especially important for hydrophobic drugs<sup>[5]</sup> or

## 1. Introduction

Nanomedicine and the wide variety of nanomaterials designed up to date have the potential to enable novel modalities for diagnosis and therapy. The complex treatment of several diseases

L. Uson, C. Yus, S. Irusta, T. Alejo, M. Arruebo, R. Arenal, V. Sebastian  
Instituto de Nanociencia y Materiales de Aragón (INMA)  
CSIC-Universidad de Zaragoza  
Zaragoza 50009, Spain  
E-mail: arruebom@unizar.es; victorse@unizar.es

L. Uson, C. Yus, S. Irusta, T. Alejo, A. Larrea, M. Arruebo, V. Sebastian  
Department of Chemical Engineering  
University of Zaragoza  
Campus Río Ebro-Edificio I+D  
C/ Poeta Mariano Esquillor S/N  
Zaragoza 50018, Spain

 The ORCID identification number(s) for the author(s) of this article can be found under <https://doi.org/10.1002/adfm.202106932>.

© 2021 The Authors. Advanced Functional Materials published by Wiley-VCH GmbH. This is an open access article under the terms of the Creative Commons Attribution-NonCommercial-NoDerivs License, which permits use and distribution in any medium, provided the original work is properly cited, the use is non-commercial and no modifications or adaptations are made.

DOI: 10.1002/adfm.202106932

L. Uson, G. Mendoza, S. Irusta, T. Alejo, M. Arruebo, V. Sebastian  
Networking Research Center on Bioengineering  
Biomaterials and Nanomedicine  
CIBER-BBN  
Madrid 28029, Spain

G. Mendoza, D. García-Domingo  
Aragon Health Research Institute (IIS Aragón)  
Zaragoza 50009, Spain

E. Leroy  
Université Paris-Est  
Institut de Chimie et des Matériaux Paris-Est  
UMR 7182 CNRS – UPEC  
2 Rue H. Dunant, Thiais 94320, France

R. Arenal, V. Sebastian  
Laboratorio de Microscopías Avanzadas  
Universidad de Zaragoza  
Zaragoza 50018, Spain

R. Arenal  
ARAID Foundation  
Zaragoza 50018, Spain

2) by facilitating the diffusion through biological membranes.<sup>[6]</sup> Drug release must be controlled and maintained at therapeutic levels, by adjusting the composition of the polymer matrix used as drug carrier and the drug loading. For this purpose, it is necessary to control several parameters in the polymeric NPs used as drug carriers: their chemical composition, size, polydispersity, architecture, surface chemistry, including hydrophilicity, hydrophobicity, and charge density.<sup>[2]</sup> Compared to other drug vectors, such as liposomes, polymeric NPs allow increasing the stability of carried drugs and control their release due to the possibility of adapting their size, structure, and chemical composition.<sup>[7]</sup>

Poly lactic-co-glycolic acid (PLGA) is a widely used polymer in drug delivery due to its biodegradability and demonstrated biocompatibility.<sup>[8]</sup> PLGA is the most common synthetic biopolymer approved by the Food and Drug Administration (FDA) and the European Medicine Agency in drug delivery systems and devices because it allows a sustained drug delivery thanks to its controlled hydrolytic degradation and the encapsulation of hydrophilic and hydrophobic therapeutic molecules.<sup>[9]</sup> Furthermore, PLGA commercially exists in different compositions to modulate its degradation kinetics and its properties are easily modifiable using site-specific chemistry in its structure.<sup>[10]</sup> PLGA can be self-assembled into micro or nanospheres by using different synthetic procedures including emulsion-solvent evaporation, nanoprecipitation, spray drying, solvent displacement, salting out, etc.

The combination of biocompatible polymers and metal NPs as hybrid nanostructures can perform several functions other than drug delivery, emerging as promising combination vectors in the new class of theragnostics used in highly sensitive biodetection,<sup>[11]</sup> medical imaging,<sup>[12]</sup> and triggered drug delivery.<sup>[13]</sup> Metal NPs can be either incorporated into the inner NP space or attached on the surface of the nanoentity.<sup>[11a]</sup> This type of hybrid NPs are usually produced by complex multistage procedures based on the covalent and noncovalent grafting to polymers of preformed metal NPs.<sup>[14]</sup> Although some of the reported procedures based on those previous strategies are easy to implement,<sup>[15]</sup> the loading control of metal NPs is poor and its reproducibility limited.<sup>[14b]</sup> It should be highlighted that the majority of nanomaterials targeted to medical applications cannot progress to clinical stage or to the market because large-scale manufacturing is in many cases not feasible due to complex synthesis procedures and the lack of reproducibility.<sup>[2]</sup> Consequently, our group developed in 2016 a novel procedure to circumvent the weaknesses of some of the previous production techniques.<sup>[14b]</sup> This procedure was based on the in situ reduction of metal ions loaded in the internal aqueous phase of a water-oil-water (w/o/w) polymeric double-emulsion of PLGA. After the emulsification process, the ions were reduced on demand by the citrate ions present in the emulsion using a redox process activated by temperature at soft conditions (40 °C) to preserve the polymer properties. Following this procedure, a tunable payload of spherical gold (Au) NPs (size ≈ 10 nm) could be encapsulated in each PLGA NP (size ≈ 175 nm).<sup>[14b]</sup> A further development was carried out by developing a continuous, robust, and scalable process to prepare these hybrid metal-polymeric NPs by a microchannel emulsification process.<sup>[16]</sup> In this case, a three-stage process in continuous flow was designed; the first two stages were aimed at the production of the w/o/w

PLGA double-emulsion and the loading of the reducing agent, as well as the Au precursor. Finally, the third stage was devoted to supply for 10 min the thermal energy required to activate the redox process. This procedure was able to supply a continuous production of Au-loaded PLGA hybrid NPs of 2.8 mg s<sup>-1</sup>.<sup>[16]</sup> Although the payload of Au NPs by the reported procedure was totally selective to the encapsulating PLGA NPs (100% loading efficiency), the shape of the inner Au NPs was not modulated. This issue hinders the applicability of the resulting hybrid NPs produced by the in situ procedure to further uses in nanomedicine where metal NPs of specific anisotropic shapes not only can be used as contrast agents<sup>[17]</sup> but also as therapeutic agents by transducing optical energy into thermal energy.<sup>[17a]</sup> This optical properties are attributed to a collective oscillation of electrons in the conduction band of metal NPs, this oscillation is named surface plasmon resonance (SPR),<sup>[18]</sup> and depends on NPs chemical composition, size, interparticle distance, shape, and aspect ratio.<sup>[19]</sup> Plasmonic NPs can emit light (i.e., electromagnetic radiation used in imaging applications) or absorb light and dissipate it in form of heat (applied in hyperthermia treatments).<sup>[20]</sup> Water molecules and tissues have reduced light absorption at near-infrared (NIR) wavelengths. In this case, coupling the NIR plasmon resonance absorption of some metal NPs into thermal energy has been exploited to photothermally destroy malignant cancer cells.<sup>[21]</sup> To date, only NIR sensitive metal NPs were loaded into large biodegradable polymeric microstructures,<sup>[11b]</sup> and thermoresponsive polymeric nanostructures,<sup>[13,22]</sup> but not in biodegradable nanostructures (having faster degradation kinetics, and reduced immunogenic reaction than the reported ones). These facts deemed important because size, shape, composition, and surface chemistry of nanovectors influence their behavior in biological contexts. For instance, the use of thermoresponsive polymers such as Poly(*N*-isopropylacrylamide)-PNIPAM could be a concern in terms of bioaccumulation and toxicity.<sup>[23]</sup> Vectoring in the microscale or nanoscale is also crucial, since nanomedicine applications generally demand nanovectors with reduced bioaccumulation and no immunogenicity. For instance, it has been shown that nanovectors smaller than 30 nm can diffuse into systemic circulation following administration into the lungs.<sup>[24]</sup> Then, the design of a simple procedure able to selectively load NIR sensitive NPs into a biopolymeric matrix, such as PLGA, at the nanoscale should be deemed important as a theragnostic nanotool.

We present here a novel and simple method to embed NIR sensitive palladium (Pd) metal nanosheets (NSs) of 1.5 nm thickness in PLGA NPs by an in situ production process. This novel approach is based on the gas-phase reduction of the metal ions loaded in the polymeric NPs by a reactive gas atmosphere with a dual role: 1) reduction agent and 2) capping agent to modulate the shape of metal nanostructures. The solubility of gases is generally limited in liquid media, having the benefit of leaving the reaction media at atmospheric conditions,<sup>[25]</sup> without leaving any cross-contamination that requires an extra purification process. On the other hand, the use of reducing agents added either as a payload in the emulsification media<sup>[14b]</sup> or in a post-treatment process<sup>[16]</sup> has evidenced some difficulties related to the emulsion formation and the nucleation/growth events of metal NPs; and even could irreversibly react with the bioactive encapsulated compounds.



Pd nanostructures have emerged as important materials in the field of nanomedicine due to their remarkable chemical<sup>[26]</sup> and optical properties.<sup>[27]</sup> Pd NSs have strong optical absorption in the NIR region and high photothermal conversion efficiency (52%) at 808 nm,<sup>[28]</sup> so they are excellent candidates as drug-release activation agents and to facilitate the induction of local hyperthermia.<sup>[27]</sup> On the other hand, many anisotropic Au nanostructures exhibiting NIR properties can be faded upon irradiation with high-power NIR lasers. This phenomenon occurs because the heat generated after NIR irradiation induces reshaping in the anisotropic structure, leading to the loss of the photothermal properties of the NPs and thereby inevitably imposing limitations in their practical therapeutic applications.<sup>[17b]</sup> Pd nanostructures, with a bulk melting point higher than that of Au (MPPd = 1,828 K vs MPAu = 1,337K) have been used to address this limitation.<sup>[17c]</sup> Pd nanosheets with a thickness of 1.5 nm were assembled in this work inside of PLGA NPs with unprecedented precision and with a 100% loading efficiency. The incorporation of metallic NPs that respond to external stimuli such as NIR light, allows the creation of triggered drug delivery systems that upon activation can provide precise control over time, dose, and location of drug administration. In addition, in this work the photothermal effect induced by NIR SPR absorption was investigated as a therapeutic nanotool.

Integrating Pd NSs, as plasmonic nanomaterials, with polymers can improve the biocompatibility, biosafety, and blood circulation half-life of these nanostructures.<sup>[29]</sup> Pd NSs heating can cause deformations in the PLGA matrix, which vitreous transition temperature range between 45 and 50 °C,<sup>[30]</sup> and could induce the release of the encapsulated drug on demand.<sup>[31]</sup> Currently, the most common activation systems are those that use UV–VIS light, which require a large amount of applied energy, which allows activating the administration systems by modifying their chemical structures. However, this light is phototoxic (UVB, UVC) and has low penetration into the tissues, which only allows its use near the surface.<sup>[32]</sup> As an alternative, the emergent option is the radiation in the NIR (700–1000 nm), range in which the majority of the absorbers in living systems show minimal absorption.<sup>[33]</sup> In addition, it has less delivered energy, so it is less harmful to cells.

Therefore, the hybrid NPs produced in this work were endowed with a triple functionality to: i) Improve drug solubility and bioavailability, ii) modify the drug release on demand at the point of action, and iii) achieve local hyperthermia, due to NIR light absorption, that produces localized cytotoxic heat able to ablate cells. In this work, the drug encapsulation study was carried out using bupivacaine, a known anesthetic molecule that at low pH is protonated, and therefore has a hydrophilic character (pKa 8.4), whereas if the pH is increased, it becomes more hydrophobic.<sup>[34]</sup> The release mechanism of PLGA/Bupivacaine systems was previously studied,<sup>[35]</sup> although the proposed hybrid nanosystem allows in addition a sustained release provided by the biodegradation of PLGA as well as the fast supply of drug on demand through a NIR laser activation and local hyperthermia. Bupivacaine was selected as a model drug being one of the most common local anesthetics used in peripheral nerve block. Most of the prolonged duration nanoparticulated carriers containing local anesthetics (such as

bupivacaine) produce a constant release profile providing a continuous extended nerve blockade without allowing for changes in the patient's daily physical activity or level of pain relief. In most of those systems the anesthetic release does not cease until all the payload is depleted. To overcome such limitation, triggerable drug delivery systems, as the one here reported, have been developed.

## 2. Results and Discussions

### 2.1. Production of Hybrid Pd-PLGA NPs

Pd NSs have been prepared in previous studies<sup>[36]</sup> using organic capping agents (i.e., cetyltrimethylammonium bromide-CTAB) to promote the anisotropic growth of Pd nanocrystals achieving the NIR absorption properties required. However, the presence of CTAB during the emulsification process, as a quaternary ammonium surfactant, can alter the w/o/w emulsion formation, besides CTAB is quite toxic to cells at sub-micromolar doses.<sup>[37]</sup> Thus, considering some of our previous results of Pd NSs growth without CTAB,<sup>[38]</sup> the synthesis of Pd NSs was adapted to a low temperature process to avoid PLGA emulsion destabilization. Pd NSs were first produced at 30 °C assisted by the capping effect of Br<sup>-</sup> ions to the (100) planes and under a pressurized atmosphere of CO (see experimental section) to increase the CO solubility in the media. The presence of CO is critical because it can supply electrons to reduce Pd<sup>2+</sup> ions to Pd<sup>0</sup> atoms and prevents the growth of Pd crystals along (111) because CO strongly adsorbs on basal (111) planes of Pd nanosheets.<sup>[36a]</sup> **Figure 1a,b** corresponds to representative transmission electron microscope (TEM) images of Pd NSs produced under these synthesis conditions where nonregular hexagonal shape nanocrystals of around 42 ± 5 nm were observed. Lattice fringes with an interplanar distance of 0.23 nm, corresponding to which can be ascribed to metallic Pd (111) surfaces,<sup>[39]</sup> can be observed in the high-resolution transmission electron microscopy (HRTEM) image displayed in **Figure 1c**. This is in agreement with previous TEM studies of Pd NSs and suggests that the nanocrystals are bound by two (111) basal planes.<sup>[36]</sup> The presence of stacked nanosheets (see **Figure 1d**) enables thickness measurement of the ultrathin structure, resulting in a mean thickness of 1.5 nm, which corresponds to less than 9 atomic layers. The ultrathin morphology of Pd NSs is crucial for their specific optical properties in the NIR region<sup>[36a]</sup> (**Figure 1j**).

As a challenge, the growth of Pd NSs was translated to the interior of PLGA NPs. The most widely used method for the synthesis of PLGA NPs is based on an emulsification process, to form the micelles of PLGA NPs, following by the evaporation of the organic solvent at room temperature to precipitate PLGA into a NP since PLGA is not soluble in water.<sup>[40]</sup> Depending on the nature of the drug to be encapsulated, simple emulsion (oil-water, o/w) for hydrophobic molecules,<sup>[41]</sup> or double emulsion (w/o/w)<sup>[42]</sup> for hydrophilic ones are commonly used. Herein, the Pd NSs reagents (hydrophilic) were loaded in the internal water compartment of the w/o/w micelles, being separated from the continuous aqueous phase by the organic layer of acetyl acetate, where PLGA is dissolved (**Figure 2a**). Sodium cholate hydrate was selected as surfactant in the w/o/w interface. Then, the Pd NSs reagents were confined in

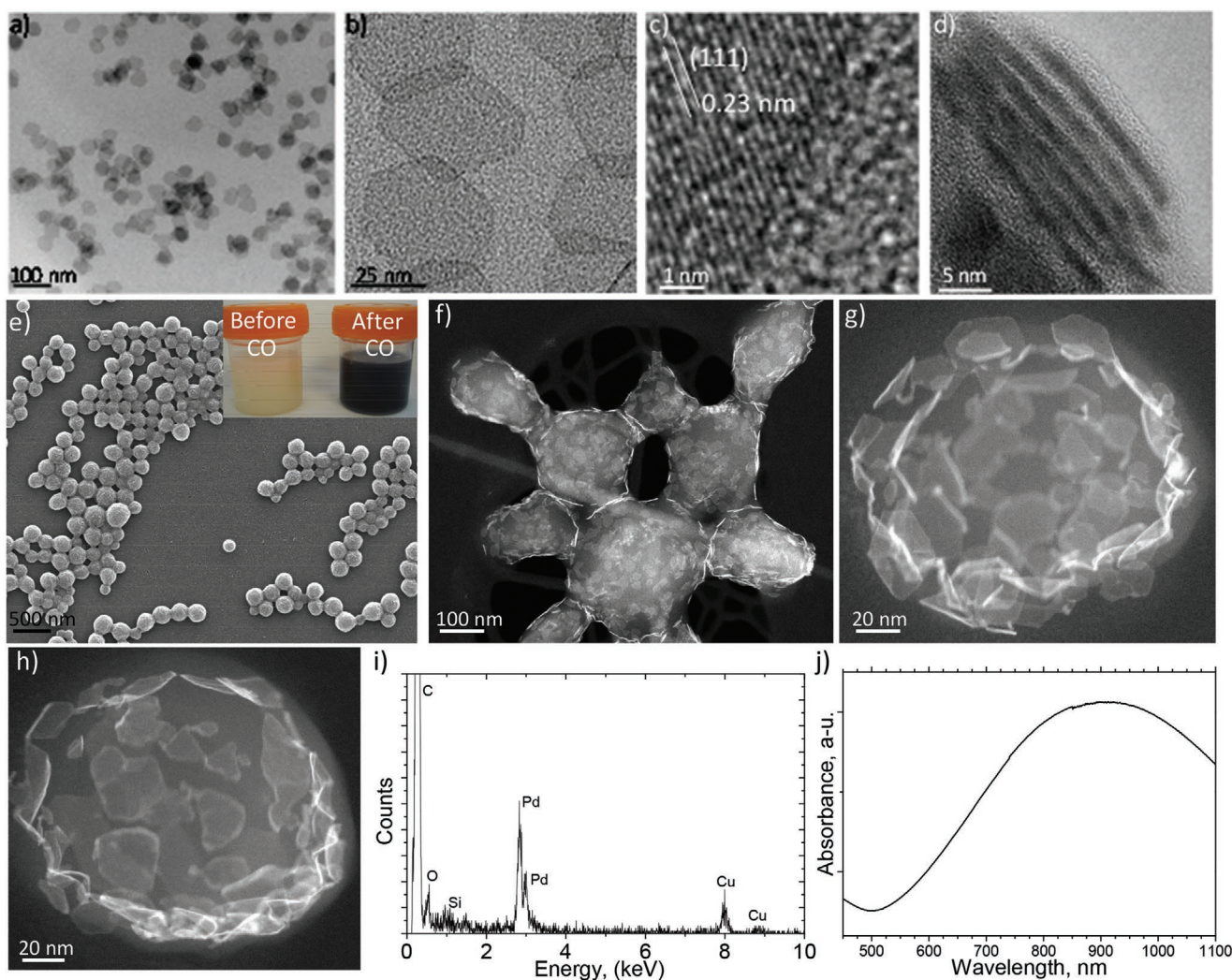


**Figure 1.** a) TEM image of Pd NSs produced with CO pressure of 6 bar after 40 min at 30 °C. b) High magnification image of a Pd NS to show its hexagonal structure. c) HRTEM image of a Pd NS showing lattice fringes, the *d*-spacing corresponds to Pd (111). d) Stack of Pd NSs located perpendicular to the TEM grid. e) SEM image of PLGA NPs loaded with Pd NSs. Inset, optical images of the Pd-PLGA emulsion before and after the gas-phase CO treatment. f) Representative HAADF-STEM image of a PLGA NP loaded with Pd NSs to show the selective growth of Pd inside PLGA NPs and no in the interparticle space. g, h) High magnification HAADF-STEM images of Pd-PLGA NPs to observe the spherical assembly of Pd NSs. i) Energy-dispersive X-ray spectrum of a Pd-PLGA NPs to determine the presence of Pd inside PLGA NPs. j) UV-vis NIR Spectrum of Pd NSs dispersed in water.

micelle like nanoreactors where the nucleation and growth events would proceed as soon as an electron donor was introduced to transform high soluble Pd ions into nonsoluble Pd atoms.

The emulsion was introduced immediately after its formation in a CO-pressurized autoclave and was kept at 30 °C for 40 min (see the Experimental Section). The ethyl acetate layer in the micelles should not be evaporated before CO treatment because its evaporation would promote the release of Pd<sup>2+</sup>/Br<sup>-</sup> ions to the continuous aqueous phase, precluding the proper assembly of Pd NSs inside PLGA NPs (Figure 2a).

Figure 1e depicts a representative scanning electron microscope (SEM) image of PLGA NPs where Pd NSs were assembled by this novel and simple procedure. Particle size histograms determined by dynamic light scattering show that the size of PLGA NPs slightly increased when Pd NPs were embedded in their interior, (182 ± 62 nm without Pd and 197 ± 43 nm with Pd loaded NSs,

respectively) (Figure S1a,b, Supporting Information). The inset in Figure 1e also shows the hue of the emulsion before and after CO treatment. The Pd-Br complex shows the typical orange color, whereas the presence of Pd NSs turns the emulsion into a dark bluish hue. It should be highlighted that Pd NSs can be formed in only 150 s when the Pd<sup>2+</sup> reduction is performed in a microfluidic system at high temperature (150 °C),<sup>[36b]</sup> but in this case a large reduction time was required (40 min) because the process occurs at low temperature (30 °C) and CO should diffuse through several water/organic layers that conform the w/o/w PLGA micelle (Figure 2). Figure 1f shows a representative high-angle annular dark-field scanning transmission electron microscopy (HAADF-STEM) image of Pd-PLGA NPs, where it is depicted that Pd NSs grow selectively only in the interior of the PLGA NPs. Due to the z-contrast information provided in HAADF images,<sup>[43]</sup> Pd NSs were observed with a



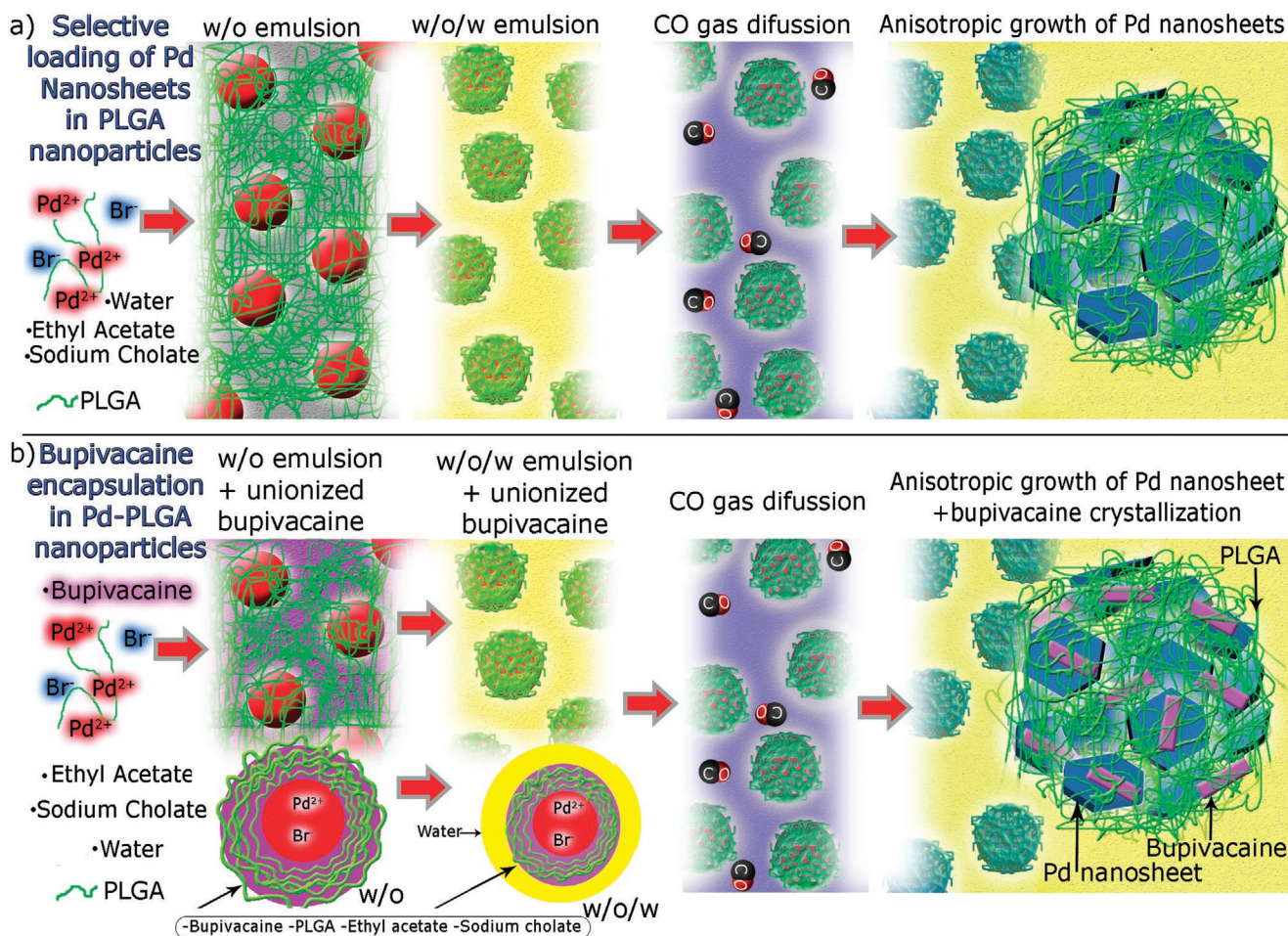


**Figure 2.** a) Scheme of the synthesis process to assemble selectively Pd NSs in PLGA NPs by a w/o/w emulsification process, assisted by a CO treatment and solvent evaporation. b) In situ encapsulation of unionized bupivacaine and Pd NSs to yield NIR triggered drug delivery systems.

brighter contrast than carbon from PLGA. Figure 1g,h shows high magnification HAADF-STEM images of some representative Pd-PLGA NPs, where it is clearly observed that Pd hexagonal and triangular NSs are assembled in the interior of PLGA NPs having an unprecedented spherical pattern of assembly. Energy-dispersive X-ray spectroscopy (EDS) confirmed the presence of Pd atoms (Figure 1i). Besides the need of using CO to control the reduction of Pd<sup>2+</sup> and the anisotropic growth of Pd NSs, the presence of Br<sup>-</sup> ions is critical to produce a homogenous nanosheet morphology. Indeed, the absence of Br<sup>-</sup> ions in the micelle during the emulsification process produces a combination of nanowires and heterogeneous NSs (Figure S2, Supporting Information). This result is in agreement with previous works,<sup>[36a]</sup> where the presence of Br<sup>-</sup> ions was justified because they regulate the lateral growth rate of Pd NSs thanks to their selective binding to the (100) planes.

## 2.2. Production of Hybrid Bupivacaine-Pd-PLGA NPs

Considering that Pd NSs were successfully embedded in the interior of PLGA, the following step was to encapsulate a therapeutic

drug without modifying the growth of Pd NSs and keeping the NIR sensitive functionality (Figure 2b). Ionized and unionized bupivacaine forms were loaded during the emulsification process (see the Experimental Section) following some of our previous protocols.<sup>[44]</sup> Unionized bupivacaine-*uiBup* (bupivacaine free base), due to its hydrophobic nature, was loaded in the organic phase of the w/o/w emulsion together with the dissolved PLGA polymer (*uiBup*-Pd-PLGA). Contrarily, ionized bupivacaine-*iBup* (bupivacaine hydrochloride), with a more hydrophilic nature than the bupivacaine free base, was loaded in the internal aqueous compartment of the w/o/w micelle, together with the Pd reagents (*iBup*-Pd-PLGA). This step is also critical because the drug could alter the emulsion stability or even block the growth of metal NPs because it could be strongly adsorbed on Pd nanocrystal facets hindering the specific CO/Br<sup>-</sup> adsorption or the growth.

Pd-PLGA NPs without drug showed a negative zeta potential value ( $-30.28 \pm 3.2$  mV) at neutral pH, whereas *uiBup*-Pd-PLGA NPs loaded with unionized bupivacaine showed positive values ( $21.43 \pm 2.9$  mV). The negative charge of pure PLGA NPs could be attributed to the presence of ionized carboxyl groups of sodium cholate surfactant on the PLGA NP surface.<sup>[45]</sup> However, the positive charge of *uiBup*-Pd-PLGA NPs might be

due to the neutralization of the polymer charge by electrostatic interaction with the drug, and residual adsorbed bupivacaine that covers the PLGA NPs surface.<sup>[13]</sup> Particle size histograms determined by dynamic light scattering (DLS) show that the size of Pd-PLGA NPs does not increase when unionized bupivacaine was encapsulated ( $185 \pm 31$  nm) (Figure S1c, Supporting Information). The analysis of SEM images of uiBup-Pd-PLGA NPs determined a mean particle size of  $146 \pm 56$  nm, which is slightly smaller than the one obtained by DLS (Figure S3a, Supporting Information). The particle size difference observed between SEM and DLS techniques was expected and it is in agreement with the literature,<sup>[46]</sup> since PLGA-Pd NPs in DLS measurements are solvated while during SEM they are dried. Fourier transform infrared spectroscopy (FTIR) studies (Figure S4, Supporting Information) were performed in order to confirm the presence of bupivacaine into PLGA NPs and the existence of possible interactions with the polymer. The FTIR spectrum of unionized bupivacaine (Figure S4a, Supporting Information) shows the absence of OH stretching band at  $3508\text{ cm}^{-1}$ , characteristic of the monohydrate drug form and the shift of the absorption band at  $3243\text{ cm}^{-1}$ , assigned to N–H stretching vibration to lower wavenumbers confirming the unionized state of the drug.<sup>[47]</sup> FTIR spectrum of bupivacaine loaded particles shows the PLGA characteristic absorption bands and also the most intense peaks of the drug (Figure S4b, Supporting Information). The small signal at  $3508\text{ cm}^{-1}$  could indicate some protonation degree of the bupivacaine after the incorporation into the particles. Comparing loaded and unloaded particles spectra, a shift for the characteristic C=O stretch ( $1756\text{ cm}^{-1}$ ) of the sodium cholate to lower wavenumbers can be observed in the uiBup-Pd PLGA spectrum.<sup>[48]</sup> On the other hand, the band associated to the presence of free carbonyl groups in bupivacaine ( $1647\text{ cm}^{-1}$ ) shifts to higher wavenumbers when loaded in PLGA particles. These facts suggest some interaction between these groups of bupivacaine with PLGA. Notice that in loaded and unloaded NPs, amide II bonds remain in the same position in the bupivacaine spectrum.

Microwave plasma-atomic emission spectrometer (MP-AES) measurements determined that palladium loading in uiBup-Pd PLGA NPs corresponded to  $17 \pm 1.9$  wt%. That is, the concentration of Pd in the sample was around  $6 \times 10^{-4}$  mg Pd per mg NPs. On the other hand, the determination of bupivacaine encapsulated in the uiBup-Pd PLGA NPs by gas chromatography-mass spectrometry (GC-MS) resulted in an efficiency of encapsulation of  $19.1 \pm 3.5$  wt% and the drug loading was  $7.6 \pm 1.8$  wt%. This value is in the same order that previous publications where bupivacaine was loaded in NPs,<sup>[44,49]</sup> but in this case the additional assembly Pd nanosheets in their interior endow the PLGA NPs with an additional therapeutic nanotool.

Regarding the iBup-Pd PLGA NPs where ionized bupivacaine was loaded in the aqueous compartment (Figure 2b), the NPs size was not substantially modified in comparison with that of PLGA NPs with Pd NPs and unionized bupivacaine, obtaining by DLS a mean size of  $175 \pm 42$  nm (Figure S1, Supporting Information). On the other hand, the surface charge ( $10.30 \pm 0.8$  mV) is slightly lower than the one obtained for the NPs loaded with unionized bupivacaine ( $21.43 \pm 2.9$  mV). This fact should be related to a limited bupivacaine loading achieved in PLGA NPs when the ionized form was used. In agreement

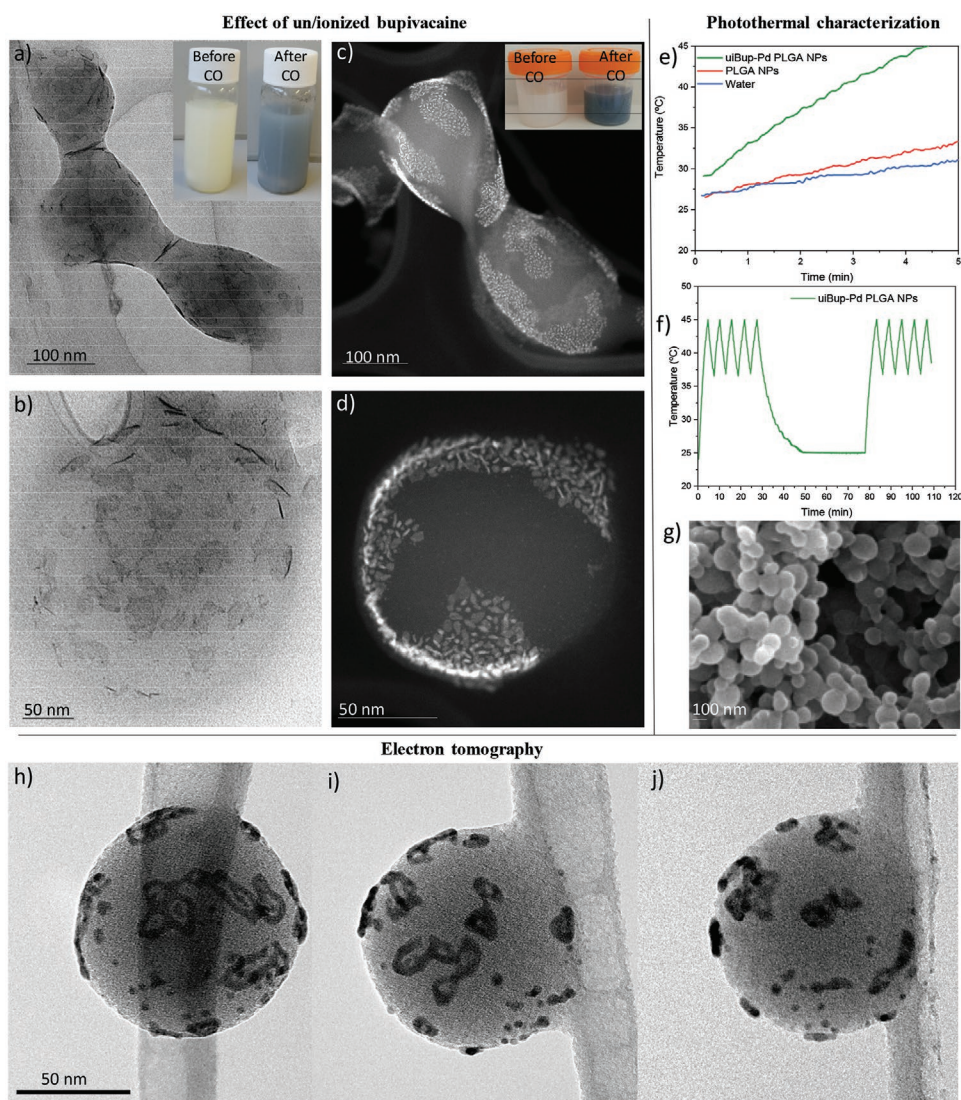
with this insight, the ionized bupivacaine quantification by CG-MS was not as high as that with the unionized type, resulting an encapsulation efficiency of  $5.52 \pm 1.2$  wt% and drug loading as low as  $0.8 \pm 0.2$  wt%. The different bupivacaine payload could be closely related with the high water-solubility of bupivacaine hydrochloride (ionized form) in comparison with the bupivacaine free base (unionized form). This is a key issue to consider in the solvent evaporation stage of PLGA NPs production, where the organic solvent release enables the polymer precipitation but also drug diffusion, reducing the encapsulated amount. In addition, the low affinity of small molecular weight hydrophilic/ionized drugs with the polymer can result in a low entrapment efficiency and a limited drug loading.<sup>[50]</sup> The simultaneous loading of iBup and uiBup was also attempted, but the loading results did not overpass the one produced with uiBup and it was not further considered.

Figure 3 depicts representative electron microscopy images of Pd-PLGA NPs encapsulating either unionized (Figure 3a,b) or ionized bupivacaine (Figure 3c,d). It can be observed that the assembly of Pd NSs in presence of unionized bupivacaine is similar to the case where no bupivacaine was used (Figure 1). However, the geometrical shape of Pd NSs was more heterogeneous than that without bupivacaine. It could be rationalized by the low solubility of unionized bupivacaine in water ( $40\text{ mg L}^{-1}$ ),<sup>[51]</sup> favoring the mere interaction with Pd NSs facets during the growth process. Regarding the assembly of Pd NSs when ionized bupivacaine was encapsulated, Figure 3c,d shows that both the dimension and shape, as well as the distribution of the NSs, were substantially modified regarding previous commented scenarios. This result is a clear evidence that ionized bupivacaine is interacting during the NSs growth, evidencing the challenge of growing nanocrystals under the presence of some drugs and the importance of selecting the proper loading scenario in the production of hybrid nanomaterials. In this case, loading the drug in a different compartment from the Pd precursor seems to avoid conflicts during the nucleation/growth events of Pd NSs. Then, Pd-PLGA loaded with unionized bupivacaine (uiBup-Pd PLGA) was selected for further analysis and for its application in triggered drug release and optical hyperthermia.

### 2.3. 3D Structure and Assembly of Hybrid Bupivacaine-Pd-PLGA NPs

To shed light on the 3D distribution of Pd NSs in the hybrid uiBup-Pd PLGA NPs, we have performed electron tomography under cryogenic conditions. Indeed, these are the most appropriated conditions to work on polymeric nanosystems as these ones, which are very sensitive to the electron beam and the damage would avoid extracting such information.<sup>[52]</sup> Thus, cryo-electron tomography at  $-170\text{ }^\circ\text{C}$  has been recorded on this system. The images from the tilt series (Figure 3h–j; and Movie S1, Supporting Information) show the spherical morphology of the PLGA-bupivacaine polymer and the 3D distribution of the Pd NSs on this polymer. They confirm that the Pd NSs are located at the shell of the PLGA NP. This finding is not reported yet in the in situ production of hybrid nanomaterials at the nanoscale level and is very interesting since the Pd precursors were loaded at the core of the NP using a double emulsion approach (Figure 2).





**Figure 3.** Electron microscopy images of Pd-PLGA NPs loaded with: a,b) unionized bupivacaine and c,d) ionized bupivacaine. Insets, optical images of the Pd-PLGA-Bupivacaine emulsions before and after the gas-phase CO treatment. e) Photothermal characterization. Temperature variation under 808 nm laser irradiation ( $1.8 \text{ W cm}^{-2}$ ,  $2.4 \text{ mg mL}^{-1}$  of NPs) for 5 min. Heating rate of Pd-PLGA NPs loaded with unionized bupivacaine, PLGA NPs without Pd (control 1) and water (control 2). f) Photothermal stability of Pd-PLGA bupivacaine NPs during 10 successive irradiation cycles with heating from 37 to 45 °C. g) SEM image of Pd-PLGA bupivacaine NPs after 10 successive irradiation cycles. h–j) TEM images of a uiBup-Pd PLGA-bupivacaine at  $-67^\circ$ ,  $0^\circ$ , and  $+67^\circ$  relative to the electron beam.

Pd nanosheets produced at the core of the w/o/w double emulsion could segregate at the interface of immiscible ethyl acetate-water interphase. This segregation would be governed by a decrease in interfacial energy as driving force. The Pd nanosheets get adsorbed onto the organic-aqueous interface and hence, the residual interfacial energy of the interfacial polymeric molecules would be released.<sup>[53]</sup> Due to the anisotropic structure of Pd NSs and the physisorption nature of this process, formation of Pd NSs monolayer at the interface is favored by the reduction in surface energy.<sup>[53]</sup> This mechanism has been well-documented in emulsion-related literature as Pickering emulsions.<sup>[53]</sup> However, this is the first time that a Pickering double emulsion is prepared at the nanometer scale without the need of first engineer the inorganic nanoconstructs before

their loading in the emulsion. The self-assembly of nanoparticles in 3D has been only developed in colloidal microcapsules because at the submicrometer scale, the nanoscale particles are characteristically unstable at the interface due to thermal disorder.<sup>[54]</sup> Consequently, the achieved results are remarkable and the proposed new procedure for hybrid nanomaterials production is a seminal route to nanoscale assemblies.

#### 2.4. Photothermal Properties: Light Triggered Drug Delivery and Thermal Ablation

The photothermal properties of uiBup-Pd PLGA NPs induced by the unique NIR SPR absorption of Pd NSs, considering that



Pd only when having sheet-like morphology is able to display its characteristic SPR absorption in the NIR region of the electromagnetic spectrum, was studied by monitoring the temperature of an aqueous solution (1 mL, 2.4 mg mL<sup>-1</sup> of NPs) irradiated by a NIR laser (808 nm, 1.8 W cm<sup>-2</sup>). As it can be observed in Figure 3e,f, a dispersion of uiBup-Pd PLGA NPs with a content in Pd of 1.45 µg mL<sup>-1</sup> increases the temperature from room temperature conditions (25 °C) to 45 °C in 5 min after irradiation. The resulting heating properties are attributed to the SPR of Pd nanosheets absorbing the NIR electromagnetic radiation in an efficient manner. In comparison, the temperature of the dispersion in absence of NPs or Pd NSs increased only 5 °C (Figure 3e,f) due to the particle scattering and the reduced energy absorption of water and PLGA in the NIR region.<sup>[27]</sup> The efficient transduction of light into heat was therefore preserved even after encapsulating the light-absorbing Pd NSs within the polymeric matrix. The stability of the NPs under laser irradiation was confirmed by performing ten successive irradiation cycles (Figure 3e,f). The suspension cooled down to body temperature in only 3 min after turning the light off, which makes these NPs potentially interesting for pulsatile photothermosensitive applications as triggered drug delivery vectors. SEM images were analyzed to evaluate if NPs morphology had changed. Figure 3g; and Figure S3 (Supporting Information) shows that the uiBup-Pd-PLGA NPs size distribution does not change after laser irradiation, although the NPs were more agglomerated after heating.

Figure 4 displays the release profile of unionized bupivacaine from uiBup-Pd PLGA NPs. Bupivacaine release present two stages: 1) an initial burst release of the entrapped drug probably close to the surface of the NPs (50% of bupivacaine is release after 5 h) and 2) a lag phase, when bupivacaine was slowly released (55% of the total bupivacaine load at 21 h), as observed with other PLGA-based particles for sustained drug delivery applications.<sup>[35b,55]</sup> The release profile was fitted to a Korsmeyer–Peppas diffusion model (Figure S5, Supporting Information) by calculating the transport exponent ( $n = 0.2$ ) and transport constant ( $K = 0.1767 \text{ h}^{-0.2}$ ). Y-axis intercept (0.41)

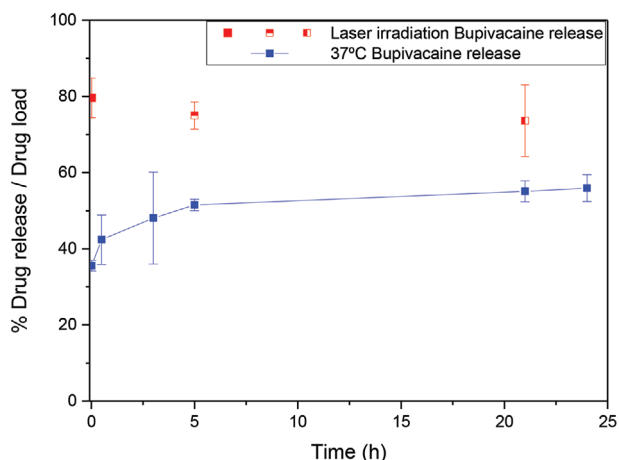


**Figure 4.** Bupivacaine release from uiBup-Pd PLGA NPs at 37 °C (blue profile) and after 5 cycles of heating-cooling from 37 to 45 °C by laser irradiation (808 nm, 1.8 W cm<sup>-2</sup>, 2.4 mg mL<sup>-1</sup> of NPs) of 3 independent samples. Percentages are displayed as mean ± SD ( $N = 3$ ).

is characteristic of the burst effect.<sup>[56]</sup> This burst initial release has been attributed to either the presence of nonencapsulated drug molecules on the surface of the NPs or to drug molecules that are located close to the external surface, but embedded in the polymer matrix.<sup>[57]</sup> The correlation coefficient ( $R^2 = 0.984$ ) was rather high that indicates a good correlation with experimental data, and the transport exponent lower than 0.5 indicates a Fickian diffusion release from a nonswellable matrix.<sup>[58]</sup> The sustained release of bupivacaine without light irradiation is caused by the erosion of the PLGA NPs due to the hydrolytic degradation of the ester bonds present in its backbone.<sup>[59]</sup>

As it is noted in Figure 4, laser irradiation caused a fast release of the 75% of the loaded drug ( $\approx 200$  ppm) after 5 heating-cooling cycles. This can be attributed to the destabilization of PLGA because its glass transition temperature ( $T_g$ ) is around 40 °C and it decreases over time.<sup>[60]</sup> Below the  $T_g$ , the polymer has limited mobility and low diffusion rates, and above it the polymer presents high water and drug transfer rates throughout the matrix.<sup>[61]</sup> So when the NPs are irradiated and reach 45 °C bupivacaine release increases due to a high diffusion rate being the thermal degradation of the polymer promoted. In addition, the interaction among drug-polymer evidenced by FTIR analysis (Figure S4, Supporting Information) diminishes with increasing temperature, in agreement with the previous literature.<sup>[62]</sup> Finally, Figure 4 displays bupivacaine release of three different samples after 5 heating-cooling cycles activated by laser irradiation and at a release time of 0, 5, and 21 h, respectively. The drug released activated function was preserved in this time interval, concluding that uiBup-Pd PLGA NPs are stable light triggered drug delivery systems during the tested timeline.

Furthermore, in order to corroborate the stability of the nanoparticles in a simulated biological medium, we have evaluated in vitro drug release in PBS supplemented with 10% fetal bovine serum (FBS). In addition, we have evaluated the long-term stability of the NPs (7 days) using SEM and TEM (Figure S6, Supporting Information). Results show a sustained release of bupivacaine during 24 h, which indicates that nanoparticles are stable without premature degradation. According to SEM and TEM images, morphology and size of the nanoparticles do not change over time.

## 2.5. In Vitro Photothermal Effects: 2D and 3D Cells Models

Figure S7 (Supporting Information) shows the in vitro cytotoxic effects of Pd-PLGA NPs on B16F1 (mouse melanoma cells), THP-1 (macrophages), human dermal fibroblasts, mouse mesenchymal stem cells (mMSCs) and human epidermal keratinocytes (HaCat) cultures.

The treatment of B16F1 and macrophages cells with the NPs did not exert cytotoxic effects at the concentration range assayed (0.02–2 mg mL<sup>-1</sup>) displaying viability percentages above 70%, which is considered as noncytotoxic according to the ISO 10993-5.<sup>[63]</sup> Moreover, macrophages did not show any effect after treatment for 24 h as their viability was the same as the one obtained for the nontreated samples (control samples). However, the NPs displayed cytotoxic effects at the higher concentrations assayed (1 and 2 mg mL<sup>-1</sup>) on HaCat,

fibroblasts, and mMSCs cells, resulting in viability percentages around 40–60%. It should be noticed that the potential interference of the Pd-PLGA NPs with the fluorescence emission reading at the highest concentration tested was also evaluated and discarded. Previous studies have also shown the cytotoxic effects of PLGA NPs loading Pd complexes ( $1\text{--}50 \times 10^{-6}$  M) in human ovarian carcinoma cell (OVCAR3) cultures after 48 h of treatment.<sup>[64]</sup> Their results showed the low cytotoxicity of Pd complexes displaying viability percentages higher than 70%. However, the nanoparticulate system exerted significant cytotoxic effects resulting in viability percentages around 20–50% which are very different from our results as at the highest concentration assayed ( $2 \text{ mg mL}^{-1}$ ) the Pd content was around  $11.3 \times 10^{-6}$  M showing viability percentages higher than 80%. Surprisingly, the effects in their assays were not dependent on the concentration. In fact, viability percentages were higher when the concentration was increased. These authors hypothesize that this effect may be attributed to the precipitation of Pd complexes due to their low solubility in water, while their loading into PLGA NPs favoured their slow release and their interaction with cell membranes. In addition, in their study Pd is present as a complex in its ionic form but in our case, Pd is present in its elemental (nonvalent form). On the other hand, PLGA-PEG NPs were loaded with Pd and doxorubicin, and the resulting nanoparticulate system was assayed for 72 h in cancer cells (HT1080).<sup>[65]</sup> Their results demonstrated a moderate cytotoxicity with a reduction in viability of 50% when adding a concentration of  $35 \times 10^{-6}$  M to the cultures, while our assays were performed at lower concentrations ( $\leq 11.3 \times 10^{-6}$  M Pd) and for 24 h though achieving higher cell viability percentages.

Photothermal effects derived from Pd-PLGA NPs treatment of melanoma cells (B16F1) and macrophages were evaluated by fluorescence microscopy through the staining of live cells with calcein (green) and dead cells with ethidium bromide (red). B16F1 cells (Figure 5a–d) and macrophages (Figure S8, Supporting Information) photothermal damage was clearly observed in the irradiated area of each treated sample only after 5 min of irradiation. Non internalized NPs were washed out before irradiating the cultures. The treated but not irradiated samples (Figure 5a–c; and Figure S8a–c, Supporting Information) exerted high cell viability showing mostly cells stained in green (live cells), which is in accordance with the results obtained in the cytotoxicity assays described above (Figure S6, Supporting Information). However, when samples were irradiated, the central area of the wells showed a red spot (Figure 5b–d; and Figure S8b–d, Supporting Information) due to the red staining of dead cells mediated by ethidium bromide. This effect seems to be more evident when the concentration was increased.

Figure S8b–d (Supporting Information) shows irradiated macrophages treated with 0.5 and  $1 \text{ mg mL}^{-1}$  of Pd-PLGA NPs, respectively. The red spot is slightly wider in Figure S8d (Supporting Information) ( $1 \text{ mg mL}^{-1}$ ) and cell mortality is higher in the surrounding area compared to Figure S8b (Supporting Information) ( $0.5 \text{ mg mL}^{-1}$ ) as red stained cells show. These results point to a dose dependent effect of the treatment with Pd-PLGA NPs after irradiation. Furthermore, melanoma cells (Figure 5a–d) displayed low viability after NP treatment and NIR irradiation as it is shown in Figure 5b–d. Indeed, a red spot is not observed in these samples due to the high mortality,

which may involve the complete loss of cell adherence and thus, their elimination when cells were washed prior to microscopy visualization. These data are in accordance with the cytotoxicity assays explained above as melanoma cells were more sensitive to NP treatment compared to macrophages, which images (Figure S8b–d, Supporting Information) displayed the red spot in the irradiated area while not reducing considerably cell density. The dose dependent effect is also observed in melanoma samples treated with Pd-PLGA NPs and NIR irradiated as clearly demonstrates the lowest cell density at the highest concentration assayed ( $1 \text{ mg mL}^{-1}$ ; Figure 5d). It is important to point out that the thermal effect did not macroscopically affect the whole well as the temperature increase measured was only  $2 \text{ }^\circ\text{C}$ ; therefore, the photothermal effect was confined on the irradiating spot area due to the coherent character of the laser beam.

Finally, the photothermal effects in B16F1 cells were evaluated by flow cytometry after treatment with Pd-PLGA NPs and NIR irradiation (Figure S9, Supporting Information). We observed that under subcytotoxic doses ( $1 \text{ mg mL}^{-1}$ ) no statistically significant changes on cell cycle were observed when treating the cells with just the NPs, just the NIR light (at the required irradiances to generate optical hyperthermia) or with the combination of both nanoparticles and NIR light. No changes in apoptosis (early, late apoptosis, and necrosis) compared to untreated controls were observed either. Finally, no caspase 3 activation was detected by flow cytometry (data not shown). All in all, those results highlight the benign character of our NPs on the nontreated cells. After performing optical hyperthermia with those NPs on the metastatic melanoma cell line, all dead cells affected by the transduced heat were detached from the wells (being adherent cells when alive) and those dead cells were removed in the washing followed during the trypsin treatment used prior cell cytometry analysis. Some of the unaffected cells that remained adhered on the wells (those far away from the irradiating light spot) were the ones collected and evaluated by flow cytometry. We observed no changes in cell cycle of apoptosis induction or caspase 3 activation highlighting the lack of collateral effects and the benefits of the spatiotemporal control of the optical hyperthermia here described.

After validating the photothermal activity of Pd-PLGA NPs in B16F1 and in macrophages as 2D cultures, the same assay was performed in 3D cell spheroids. Spheroids can mimic the environment and the interactions between cells of tumors.<sup>[66]</sup> Moreover, spheroids have been widely accepted as models of study for drug delivery systems<sup>[67]</sup> or photothermal therapy.<sup>[68]</sup> In this work, B16F1 spheroids were used to evaluate the *in vitro* efficiency of Pd-PLGA NPs combined with irradiation in photothermal therapy. In agreement with the results obtained in the 2D model, the Pd-PLGA NPs treatment without irradiation did not produce any cytotoxic effect on the spheroids (Figure 5f), showing mostly green stained cells (live cells), as the nontreated and nonirradiated control spheroids (Figure 5e). Figure 5g,h shows treated and irradiated samples with 0.5 and  $1 \text{ mg mL}^{-1}$  of Pd-PLGA NPs, respectively. Treated and irradiated spheroids displayed high cell mortality showing mostly cells stained in red (dead cells). In accordance to the 2D assay, the photothermal effect was dependent on the NPs concentration exerting higher cell mortality after treatment with



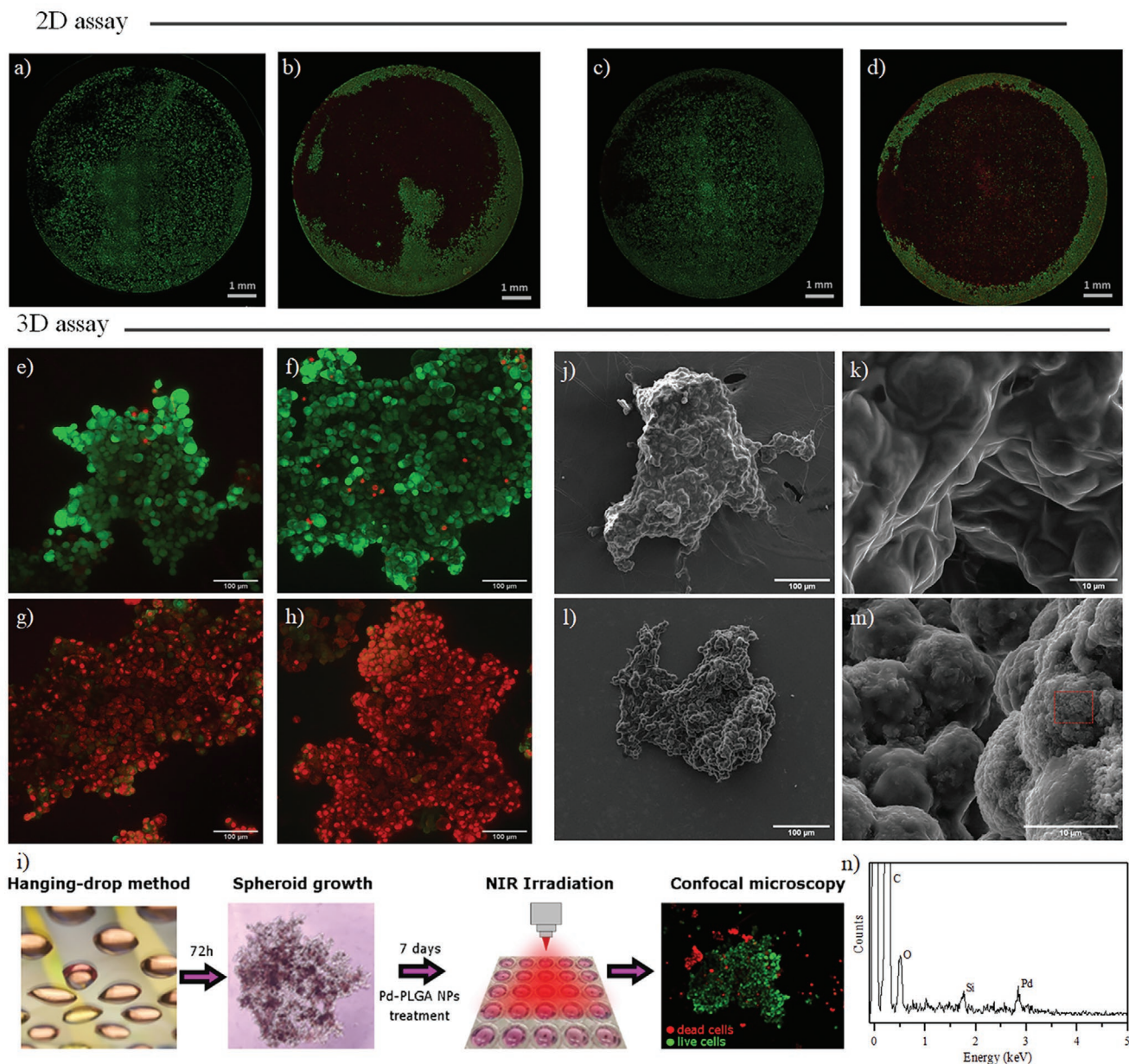


**Figure 5.** 2D photothermal effects on B16F1 cells a–d) after treatment with Pd-PLGA NPs. Composition of pictures (144 fields, 5x magnification) to show the whole cell culture well. a) cells treated with  $0.5 \text{ mg mL}^{-1}$  Pd-PLGA NPs, not irradiated; b) cells treated with  $0.5 \text{ mg mL}^{-1}$  Pd-PLGA NPs and irradiated for 5 min; c) cells treated with  $1 \text{ mg mL}^{-1}$  Pd-PLGA NPs, not irradiated; d) cells treated with  $1 \text{ mg mL}^{-1}$  Pd-PLGA NPs and irradiated for 5 min. Cells were observed under a fluorescence microscope, showing live cells in green and dead cells in red. 3D photothermal effects on B16F1 spheroids e–h) after treatment with Pd-PLGA NPs. e) Spheroid not treated and not irradiated; f) spheroid treated with  $1 \text{ mg mL}^{-1}$  Pd-PLGA NPs, not irradiated; g) spheroid treated with  $0.5 \text{ mg mL}^{-1}$  Pd-PLGA NPs and irradiated for 5 min. h) Spheroid treated with  $1 \text{ mg mL}^{-1}$  Pd-PLGA NPs and irradiated for 5 min. Spheroids were observed under a confocal microscope at 25x magnification, showing live cells in green and dead cells in red. i) Schematic representation of the photothermal therapy in the 3D cell model. SEM images of 3D B16F1 spheroids j–m). j,k) Spheroid not treated and no irradiated; l,m) Spheroid treated with  $1 \text{ mg mL}^{-1}$  Pd-PLGA NPs, not irradiated. n) Energy-dispersive X-ray spectrum of the spheroid surface marked with a red dashed line in m).

$1 \text{ mg mL}^{-1}$  NPs suspensions. Figure 5i showed the scheme of the procedure performed. 2D and 3D experiments clearly illustrate the potential of this hybrid nanomaterial as a photothermal nanotool upon exposure to NIR light.

Nontreated and nonirradiated spheroids' morphology and size did not show any differences in comparison with treated

spheroids (Figure 5i–l). Figure 5l revealed mostly of Pd-PLGA NPs in the surrounding of the spheroid. The presence of Pd into the surface of the spheroid was confirmed by energy-dispersive X-ray spectroscopy (EDS) analysis (Figure 5n). The accumulation of PLGA NPs in the periphery of the spheroid was reported in previous works showing a higher presence

of PLGA NPs attached to the cell wall of the spheroid and an improved internalization of PLGA NPs only when modified with L-carnitine.<sup>[69]</sup> Such accumulation can be explained by the physical barriers constituted by the high ordering and adhesion of the cells in the 3D model.<sup>[70]</sup> All the photothermal effect observed would be attributed to the light absorption caused by the internalized NPs and to the inherent cytotoxicity of the NPs themselves. Overall, Pd-PLGA NPs are expected to be potentially applied in cancer chemophotothermal therapy due to their promising capabilities.

### 3. Conclusions

We have introduced a novel and efficient method for the synthesis of hybrid PLGA NPs. The hybrid nanomaterials were synthesized by using the double emulsion solvent evaporation method and loaded with Pd NSs generated in-situ by the assistance of a gas phase reducing agent that is not only able to supply electrons but also to promote the anisotropic growth of NIR-absorbing Pd. The Pd-PLGA NPs were also loaded with hydrophobic bupivacaine as a proof of concept to be used as triggerable drug delivery system. Electron microscopy imaging techniques unveil the 3D structure of Pd NS assembly. Being this type of assembly, a novelty based on Pickering double emulsions in NPs. Importantly, the coloaded drug molecules do not significantly interfere with the Pd growing mechanism since they were initially loaded in different micellar compartments. Drug release results show a profile according to the hydrolytic erosion of PLGA NPs during 24 h, and an accelerated release on demand when NPs were irradiated with an 808 nm laser at desired time points. This release on demand occurs when the polymer reaches its rubbery state, promoting a rapid drug diffusion and a weak interaction between the PLGA chains and the drug. In vitro cytotoxic studies of the hybrid nanomaterials on B16F1 (mouse melanoma cells) and THP-1 (macrophages) cultures revealed a lack of cytotoxic effects at the concentration range assayed (0.02–2 mg mL<sup>-1</sup>). Finally, an important outcome of this study is the demonstration that this novel nanovector is a theragnostic nanotool, the Pd NSs were able of coupling the NIR plasmon resonance absorption into thermal energy to photothermally destroy malignant cancer cells. This capability was assayed using 2D and 3D cells models highlighting the NPs efficiency in chemophotothermal therapy. In addition, cell cycle studies confirmed the lack of collateral effects and the benefits of the spatiotemporal control of the optical hyperthermia here described. Since PLGA is a biocompatible and biodegradable polymer, potential applications of these hybrid nanomaterials can be foreseen in theragnostics, in particular when triggered drug delivery, medical imaging, and photothermal therapies are required.

### 4. Experimental Section

**Chemical Reagents:** The reactant materials used in the experiments were: Resomer RG 504, an ester terminated poly (D, L-lactic acid/glycolic acid) 50/50 (molecular weight 38–54 kDa), which was purchased from Evonik Industries AG (Darmstadt, Germany). Drugs including

bupivacaine hydrochloride monohydrate and (S)-(-)-limonene (as internal standard, food grade  $\geq 95\%$ ), surfactant sodium cholate hydrate (for Cell Culture, BioReagent), Potassium tetrachloropalladate (II) (Aldrich, trace metal basis,  $\geq 99.99\%$ ), Potassium bromide (ACS reagent  $\geq 99\%$ ), sodium hydroxide (ACS reagent  $\geq 97.0\%$ ), PBS, FBS, and the solvents ethyl acetate, acetonitrile, and methanol (HPLC grade) were supplied by Sigma-Aldrich Co. (St. Louis, MO).

**Synthesis of Pd-PLGA and Pd-PLGA-Bupivacaine NPs:** Pd-PLGA NPs were prepared by a water/oil/water (w/o/w) emulsion and solvent evaporation method. In this method, 50 mg of PLGA polymer were dissolved into 1 mL of ethyl acetate and emulsified with 50  $\mu$ L of palladium precursor solution (inner water phase). The palladium precursor solution was prepared by adding 3 mg of K<sub>2</sub>PdCl<sub>4</sub> and 60 mg of KBr in 100  $\mu$ L of water.

This mixture was sonicated in an ice bath for 15 s with a sonicator (Digital sonifier 450, Branson, USA) using a probe of 0.13 in. in diameter and 30% of amplitude. Then the formed w/o emulsion was emulsified with 2 mL of 10% w/v sodium cholate solution at 30% amplitude for 15 s to obtain the w/o/w emulsion. 10 mL of 0.3% w/v sodium cholate solution were also added to promote the stability of the emulsion. After the formation of a stable emulsion, the reduction of palladium precursor was carried out in order to obtain palladium nanosheets. The emulsion was introduced immediately after its formation in a CO<sub>2</sub>-pressurized autoclave and was kept at 30 °C for 40 min. The pressure of the autoclave was set at 6 bar. N<sub>2</sub> gas was flushed after the CO treatment to block the Pd reduction reaction. To achieve the formation of PLGA NPs, ethyl acetate was evaporated under continuous stirring (600 rpm) for 3 h. Finally, to remove nonreacted reagents, the mixture was washed by centrifugation, three times, at 7500 rpm for 10 min. The resulting NPs were dispersed in 2 mL of distilled water or PBS + 10% FBS for further use.

Pd-PLGA-Bupivacaine NPs were prepared with unionized bupivacaine. Bupivacaine free base (unionized bupivacaine) was prepared according to previously reported procedures with slight modifications.<sup>[64]</sup> Briefly, 20 mg mL<sup>-1</sup> of bupivacaine hydrochloride solution was deprotonated by addition of 0.2 M NaOH solution dropwise under vigorous stirring. The NaOH was added until the pH of the solution was adjusted to 11, above the pK<sub>a</sub> of the molecule (pK<sub>a</sub> = 8.4). The solution turned to cloudy and subsequently the free base form precipitated as a white solid in the solution. The excess of salts was eliminated filtering the solid under vacuum and by several cycles of washing with distilled water. Afterward, bupivacaine free base was dried under vacuum.<sup>[71]</sup> To prepare these NPs, 10 mg of bupivacaine were dissolved in the ethyl acetate used to dissolve the PLGA in the described protocol.

In addition, NPs with bupivacaine hydrochloride (iBup-Pd-PLGA NPs) were prepared to probe the possibility of incorporating hydrophilic drugs as mentioned before. For this, 2 mg of bupivacaine hydrochloride (ionized bupivacaine) were dissolved in the 50  $\mu$ L of palladium precursor solution used as inner aqueous phase.

**Physico-Chemical Characterization of the NPs:** Morphological characterization of the NPs was preliminarily performed using a T20-FEI Tecnai TEM and an Inspect F-50SEM (FEI, Holland), with the NPs previously coated with a carbon layer. Aberration corrected scanning transmission electron microscopy (Cs-corrected STEM) images were acquired using a high angle annular dark field detector in a FEI XFEG TITAN electron microscope operated at 300 kV equipped with a CESCOR Cs-probe corrector from CEOS. Electron cryo-tomography was acquired in a FEI Tecnai F-20 working at 200 kV and -170 °C using a GATAN cryo-tomographic holder. The acquisition was made in TEM mode with the GATAN acquisition software. The tilt angles were -67° to +67° with a 2° angular step and Saxton scheme. The reconstruction was made using Tomviz software to the alignment of the images and TomoJ for the reconstruction (OS-SART-30 iterations). The visualisation was made with ImageJ 3D Viewer.

Hydrodynamic diameter of the NPs was determined by dynamic light scattering measurements in a Brookhaven 90 Plus (Holtsville, NY) system at pH 7. The Zeta potential of NPs was determined using the Zeta Potential Analyser from Brookhaven 90 Plus (Holtsville, NY) at pH 7.



To evaluate the molecular interactions between the drug and the polymeric NPs FTIR (Vertex 70, Bruker) with ATR Golden Gate Diamond was used.

The amount of Pd incorporated onto the PLGA NPs was determined by using a microwave plasma-atomic emission spectrometer (Agilent 4100 MP-AES). Samples were previously digested, with a mixture of aqua regia and distilled water (1:9) and filtered using a 0.2  $\mu\text{m}$  PTFE filter.

The release of bupivacaine was monitored over 24 h in water and in PBS+10% FBS. NPs were stored under stirring at 37 °C inside a thermostatically controlled chamber (Model Stuart SI60D, Fisher Scientific Afora). To be analyzed, samples were centrifuged at 9000 rpm during 10 min to obtain a supernatant free of NPs.

Bupivacaine concentrations were determined by CG-MS, using a methanol solution of (s)-(-)-limonene (50 ppm) as internal standard. CG-MS measurements were carried out with a Shimadzu 2010SE GC-MS chromatograph having a Zebtron ZB-50 capillary column (30 m  $\times$  0.25 mm  $\times$  0.25  $\mu\text{m}$ , Phenomenex). Oven temperature increased from 50 to 170 °C at 30 °C  $\text{min}^{-1}$ , then rose to 250 °C with a rate of 45 °C  $\text{min}^{-1}$  and finally increased to 300 °C with a rate of 10 °C  $\text{min}^{-1}$ , maintaining this temperature for 2 min. Helium was used as carrier gas with a constant flow rate of 11.5 mL  $\text{min}^{-1}$ . Temperature of injection was 250 °C, and the ion source temperature was 200 °C. Injection volume was 1  $\mu\text{L}$  with a split ratio of 1:10. Samples were prepared by adding 150  $\mu\text{L}$  of the sample supernatant, 650  $\mu\text{L}$  of acetonitrile, 100  $\mu\text{L}$  of methanol, and 100  $\mu\text{L}$  of internal standard. In the case of the release conducted on PBS+10% FBS, sample pellet was dissolved in 800  $\mu\text{L}$  of acetonitrile, 100  $\mu\text{L}$  of methanol, and 100  $\mu\text{L}$  of internal standard. In addition, ultraviolet-visible spectroscopy (UV-vis) was used to analyze the band at 262 nm corresponding to bupivacaine.<sup>[13]</sup>

**Encapsulation Efficiency of Bupivacaine in Pd-PLGA NPs:** The amount of bupivacaine loaded in the NPs was determined analyzing, by CG-MS, the amount of drug detected in the supernatants. To evaluate the encapsulation efficiency (EE%) and the amount of bupivacaine in the NPs (DL%) these two equations were used

$$EE\% = \frac{\text{Mass of drug encapsulated in NPs}}{\text{Total mass of drug added}} \times 100 \quad (1)$$

$$DL\% = \frac{\text{Mass of drug encapsulated in NPs}}{\text{Total mass of NPs}} \times 100 \quad (2)$$

The photothermal properties of the NPs were evaluated under laser irradiation using an 808 nm laser diode (model MDL-III-808-2W, Changchun New Industries Optoelectronics Technology Co., Ltd., Changchun, P. R. China), coupled to an optical fiber of 400  $\mu\text{m}$  of diameter and a fixed focus collimator (Thorlabs, Newton, NJ). Samples, containing 2.4 mg  $\text{mL}^{-1}$  of NPs in water, were irradiated at 1.8 W  $\text{cm}^{-2}$ , under magnetic stirring until their temperature reached 45 °C. Then, they were cooled to 37 °C. The heating-cooling cycle was repeated 5 times to each sample. The amount of released bupivacaine was again measured by CG-MS.

The drug release profile was fitted to Korsmeyer–Peppas:

$$\frac{Q}{Q_{\infty}} = k \cdot t^n \quad (3)$$

Where  $Q$  is the amount released at time  $t$ ,  $Q_{\infty}$  is the overall released amount,  $k$  is a release constant, and  $n$  is a dimensionless number.

**Cell Viability, Flow Cytometry Assays, and In Vitro Photothermal Effects:** B16F1 mouse melanoma cells (kindly donated by Dr. Pilar Martin-Duque), HaCaT human keratinocytes (Lonza, Belgium), and Human dermal fibroblasts (Lonza, Belgium) were cultured in Dulbecco's modified Eagle's medium (DMEM) high glucose with stable glutamine (Biowest, France) supplemented with fetal bovine serum (FBS, 10% v/v; Thermo Fisher Scientific, USA) and antibiotic-antimycotic solution (60  $\mu\text{g mL}^{-1}$  penicillin, 100  $\mu\text{g mL}^{-1}$  streptomycin, and 0.25  $\mu\text{g mL}^{-1}$  amphotericin B; Biowest, France) at 37 °C and 5%  $\text{CO}_2$  in a humidified incubator. Mouse mesenchymal stem cells (mMSCs) (Lonza, Belgium) were cultured in Dulbecco's modified Eagle's F-12 medium (DMEM

F-12) (Biowest, France) supplemented with fetal bovine serum (FBS, 10% v/v, Thermo Fisher Scientific, MA), stable glutamine (2  $\times 10^{-3}$  M, Biowest) and an antibiotic-antimycotic (60  $\mu\text{g mL}^{-1}$  penicillin, 100  $\mu\text{g mL}^{-1}$  streptomycin, and 0.25  $\mu\text{g mL}^{-1}$  amphotericin B, Biowest) and maintained at 37 °C under hypoxic conditions (3%  $\text{O}_2$ ). THP-1 cells were purchased from the American Type Culture Collection (ATCC, TIB-202, USA) and cultured in RPMI 1640 medium with stable glutamine (Biowest, France) supplemented with 10% v/v FBS (Thermo Fisher Scientific, USA), 1% nonessential amino acids (Biowest, France), 1% sodium pyruvate (Biowest, France), 1% HEPES (Biowest, France), 0.1% 2-mercaptoethanol (Gibco, Thermo Fisher Scientific, USA), and an antibiotic-antimycotic solution (60  $\mu\text{g mL}^{-1}$  penicillin, 100  $\mu\text{g mL}^{-1}$  streptomycin, and 0.25  $\mu\text{g mL}^{-1}$  amphotericin B; Biowest, France). Both cell lines were grown at 37 °C and 5%  $\text{CO}_2$  in a humidified incubator. To carry out the in vitro experiments, THP1 cells were differentiated into the adherent macrophage-like state in supplemented RPMI 1640 medium also adding 1  $\times 10^{-6}$  M phorbol 12-myristate 13-acetate (PMA; Sigma-Aldrich, USA) for 72 h. After this time, cells clearly showed adherent morphology.

To develop the in vitro cytotoxicity assay, cells were seeded in 96-well plates (B16F1 5000 cells per well, fibroblasts 6000 cells per well, HaCat 5000 cells per well, mMSCs 5000 cells per well, and macrophages 70 000 cells per well). Then, Pd-PLGA NPs were added to the cells at different concentrations (0.02–2 mg  $\text{mL}^{-1}$ ) in supplemented medium and incubated for 24 h at 37 °C and 5%  $\text{CO}_2$ . After incubation, cells were washed twice with Dulbecco's Phosphate Buffered Saline (DPBS; Biowest, France) and the Blue Cell Viability reagent (Abnova, Taiwan) was added (10% v/v in supplemented medium) and incubated for 4h at 37 °C and 5%  $\text{CO}_2$  to elucidate the cytotoxicity of Pd-PLGA NPs based on cell metabolism effects. Then, cell viability was determined by fluorescence reading (535/590 nm ex/em; Synergy HT Microplate Reader, Biotek, USA). Viability percentages were calculated by the interpolation of the emission data obtained from treated and control samples (100% viability).

To validate the photothermal effects of Pd-PLGA NPs mediated by NIR irradiation, B16F1 cells and macrophages were seeded in 24-well plates (B16F1 40 000 cells per well, macrophages 500 000 cells per well). Then, Pd-PLGA NPs were added (0.5 and 1 mg  $\text{mL}^{-1}$ ) to the cells in supplemented medium and incubated for 24 h at 37 °C and 5%  $\text{CO}_2$ . After incubation, cells were washed twice with DPBS to eliminate extracellular NPs and thus, to evaluate only the effects of intracellular NPs. Fresh growth medium was added to the cells and NIR irradiation performed at 808 nm and 5.2 W  $\text{cm}^{-2}$  for 5 min only on the center of the well by using a laser collimator rendering a coherent beam. Then, cell damage mediated by Pd-PLGA NPs treatment and NIR irradiation was assessed by fluorescence microscopy through the Live/Dead Viability/Cytotoxicity Kit (Thermo Fisher Scientific, USA) following the manufacturer instructions. Briefly, a 2  $\times 10^{-6}$  M calcein AM and 4  $\times 10^{-6}$  M ethidium homodimer-1 solution were added to the cells. After incubation at room temperature for 30 min, cells were observed under an inverted fluorescence microscope (Widefield Time Lapse Leica AF6000 LX, Leica, Germany). The images were acquired by the composition of 144 fields per well at 5x magnification to obtain a full view of each well. Treated but not irradiated samples were also tested to compare the cell status. Moreover, control samples (not treated nor irradiated) were also assayed to test the basal status of the cells.

In order to elucidate the photothermal effects in cells, B16F1 were seeded in 24-well plates (40 000 cells per well) and treated for 24 h with Pd-PLGA NPs (1 mg  $\text{mL}^{-1}$ ) at 37 °C and 5%  $\text{CO}_2$ . Then, cells were washed with DPBS and fresh growth medium was added to the cells and NIR irradiation performed at 808 nm and 5.2 W  $\text{cm}^{-2}$  for 5 min. After irradiation, cells were harvested in PBS and cells were used in different flow cytometry experiments. A quantitative analysis of cell death by apoptosis and necrosis was performed by flow cytometry and by means of a commercial kit (Annexin V FITC kit, Immunostep) following the manufacturer's instructions. In brief, samples (10<sup>6</sup> cells  $\text{mL}^{-1}$ ) were centrifuged at 1200 rpm for 5 min and the pellet was resuspended in 100  $\mu\text{L}$  of Annexin-binding buffer. Then, samples were stained with Annexin V-FITC and propidium iodide for 15 min at room temperature in

the dark. Finally, 150  $\mu\text{L}$  Annexin-binding buffer was added to the samples and analyzed by flow cytometry. On the other hand, the distribution of the cell cycle phases was also determined by flow cytometry. After collecting cells in PBS, samples were fixed in 70% ice-cold ethanol and incubated at 4  $^{\circ}\text{C}$  for 24 h. Then, DNA was stained by adding a solution of 50  $\mu\text{g mL}^{-1}$  propidium iodide and 100  $\mu\text{g mL}^{-1}$  RNase A in PBS to be then analyzed by flow cytometry. Finally, the activation of Caspase-3 was analyzed by flow cytometry after fixing cells with 4% PFA and incubated with a FITC-labeled antibody against the active form of caspase-3 (Pharmingen) diluted in 0.1% saponin in PBS. After washing, cells were resuspended in 1% PFA and analyzed by flow cytometry. All the experiments were evaluated in a FACSAria BD equipment with the FACSDIVA BD software (Cell Separation and Cytometry Unit, CIBA, IIS Aragon, Spain). In these assays, negative controls were also run to compare the basal level of cells to that obtained after treatment, and the control samples without the cells were also analyzed to test a potential NP interference with the methodology.

**B16F1 Spheroids Generation and Photothermal Effects:** To create the B16F1 spheroids the hanging-drop method was used. 25  $\mu\text{L}$  drops of culture medium containing 2500 cells were plated on the lid of a petri dish. The petri dish was filled with sterile water to prevent the drop evaporation. After 72 h, the spheroids were collected and placed in a 96-well  $\mu\text{L}$  plate previously coated with 50  $\mu\text{L}$  of agarose (1% w/v, Condalab, Spain) and were incubated 7 days at 37  $^{\circ}\text{C}$  and 5%  $\text{CO}_2$ . The culture medium was replaced every two days. Then, Pd-PLGA NPs were added (0.5 and 1  $\text{mg mL}^{-1}$ ) to the spheroids in supplemented medium. After 24 h of incubation, spheroids were collected and washed with an excess of DPBS and irradiated at 808 nm and 5.2  $\text{W cm}^{-2}$  for 5 min. Cell damage produced by the internalized or adhered NPs was determined by fluorescence microscopy labeling the aggregated cells with the Live/Dead Viability/Cytotoxicity Kit (Thermo Fisher Scientific, USA), as mentioned before. Spheroids were observed under a confocal microscope (Confocal Zeiss LSM 880, Zeiss, Germany) with a 25 $\times$  objective. Not irradiated and not treated-not irradiated spheroids were also assayed.

For morphological visualization an Inspect F50 field emission gun scanning electron microscope was used (SEM FEI, Holland). Control and treated spheroids were fixed with paraformaldehyde (PFA) 4% in PBS (Alfa Aesar, Germany) overnight at 4  $^{\circ}\text{C}$ . Then, spheroids were dehydrated and coated with carbon layer (Leica EM ACE200, Leica, Wetzlar, Germany).

## Supporting Information

Supporting Information is available from the Wiley Online Library or from the author.

## Acknowledgements

L.U. and C.Y. contributed equally to this work. The authors thank financial support from the ERC Consolidator Grant program (No. ERC-2013-CoG-614715, NANOHEDONISM). CIBER-BBN is an initiative funded by the VI National R&D&I Plan 2008–2011 financed by the Instituto de Salud Carlos III with the assistance of the European Regional Development Fund. The (HR)TEM and STEM-EDS studies were conducted at the Laboratorio de Microscopias Avanzadas, Universidad de Zaragoza, Spain. G.M. thanks the support from the Miguel Servet Program (No. MS19/00092; Instituto de Salud Carlos III). V.S. acknowledges the financial support of Ministerio de Ciencia, Innovación y Universidades, Programa Retos Investigación, Proyecto >REF: RT12018-099019-A-I00. R.A. acknowledges funding from the Spanish MICINN (project grant PID2019-104739GB-I00/AEI/10.13039/501100011033), from the Government of Aragon (project DGA E13-20R), and from the European Union H2020 program “ESTEEM3” (No. 823717).

## Conflict of Interest

The authors declare no conflict of interest.

## Data Availability Statement

The data that support the findings of this study are available from the corresponding author upon reasonable request.

## Keywords

bupivacaine drug delivery, hybrid nanospheres, photothermal therapy, pickering double emulsion, plasmonic palladium

Received: July 17, 2021

Revised: October 14, 2021

Published online: November 23, 2021

- [1] B. Begines, T. Ortiz, M. Pérez-Aranda, G. Martínez, M. Merinero, F. Argüelles-Arias, A. Alcudia, *Nanomaterials* **2020**, *10*, 1403.
- [2] R. Duncan, M. J. Vicent, *Adv. Drug Delivery Rev.* **2013**, *65*, 60.
- [3] a) Y. Liu, L. Mao, S. Yang, M. Liu, H. Huang, Y. Wen, F. Deng, Y. Li, X. Zhang, Y. Wei, *Dyes Pigm.* **2018**, *158*, 79; b) Y. Liu, X. Wu, Y. Mi, B. Zhang, S. Gu, G. Liu, X. Li, *Drug Delivery* **2017**, *24*, 443; c) F. Novio, J. Simmchen, N. Vázquez-Mera, L. Amorín-Ferré, D. Ruiz-Molina, *Coord. Chem. Rev.* **2013**, *257*, 2839.
- [4] *Strategies to Modify the Drug Release from Pharmaceutical Systems*, (Ed: M. L. Bruschi), Woodhead Publishing, Cambridge **2015**, pp. 15–28.
- [5] a) A. George, P. A. Shah, P. S. Shrivastav, *Int. J. Pharm.* **2019**, *561*, 244; b) L. Zhao, G. Shen, G. Ma, X. Yan, *Adv. Colloid Interface Sci.* **2017**, *249*, 308.
- [6] P. R. Leroueil, S. Hong, A. Mecke, J. R. Baker Jr., B. G. Orr, M. M. Banaszak Holl, *Acc. Chem. Res.* **2007**, *40*, 335.
- [7] a) M. A. Farooq, M. Aquib, A. Farooq, D. Haleem Khan, M. B. Joelle Maviyah, M. Sied Filli, S. Kesse, K. O. Boakye-Yiadom, R. Mavlyanova, A. Parveen, B. Wang, *Artif. Cells, Nanomed., Biotechnol.* **2019**, *47*, 1674; b) M. J. Moura, M. H. Gil, M. M. Figueiredo, *Eur. Polym. J.* **2019**, *113*, 357.
- [8] I. Ortiz de Solorzano, L. Uson, A. Larrea, M. Miana, V. Sebastian, M. Arruebo, *Int. J. Nanomed.* **2016**, *11*, 3397.
- [9] L. Español, A. Larrea, V. Andreu, G. Mendoza, M. Arruebo, V. Sebastian, M. S. Aurora-Prado, E. R. M. Kedor-Hackmann, M. I. R. M. Santoro, J. Santamaría, *RSC Adv.* **2016**, *6*, 111060.
- [10] a) M. Mir, N. Ahmed, A. u. Rehman, *Colloids Surf., B* **2017**, *159*, 217; b) F. Danhier, E. Ansorena, J. M. Silva, R. Coco, A. Le Breton, V. Préat, *J. Controlled Release* **2012**, *161*, 505; c) H. K. Makadia, S. J. Siegel, *Polymers* **2011**, *3*, 1377; d) I. O. De Solorzano, L. Uson, A. Larrea, M. Miana, V. Sebastian, M. Arruebo, *Int. J. Nanomed.* **2016**, *11*, 3397.
- [11] a) M. J. Sailor, J.-H. Park, *Adv. Mater.* **2012**, *24*, 3779; b) M. S. Strozyk, D. J. de Aberasturi, J. V. Gregory, M. Brust, J. Lahann, L. M. Liz-Marzán, *Adv. Funct. Mater.* **2017**, *27*, 1701626.
- [12] E. Luque-Michel, V. Sebastian, A. Larrea, C. Marquina, M. J. Blanco-Prieto, *Eur. J. Pharm. Biopharm.* **2019**, *145*, 65.
- [13] T. Alejo, V. Andreu, G. Mendoza, V. Sebastian, M. Arruebo, *J. Colloid Interface Sci.* **2018**, *523*, 234.
- [14] a) H. Li, J. V. John, S. J. Byeon, M. S. Heo, J. H. Sung, K.-H. Kim, I. Kim, *Prog. Polym. Sci.* **2014**, *39*, 1878; b) E. Luque-Michel, A. Larrea, C. Lahuerta, V. Sebastian, E. Imbuluzqueta, M. Arruebo, M. J. Blanco-Prieto, J. Santamaría, *Nanoscale* **2016**, *8*, 6495.



- [15] Y. Qiu, R. Palankar, M. Echeverría, N. Medvedev, S. E. Moya, M. Delcea, *Nanoscale* **2013**, *5*, 12624.
- [16] A. Larrea, A. Clemente, E. Luque-Michel, V. Sebastian, *Chem. Eng. J.* **2017**, *316*, 663.
- [17] E. Luque-Michel, V. Sebastian, B. Szczupak, E. Imbuluzqueta, J. Llop, M. J. Blanco Prieto, *J. Drug Delivery Sci. Technol.* **2017**, *42*, 315.
- [18] X. Huang, M. A. El-Sayed, *J. Adv. Res.* **2010**, *1*, 13.
- [19] R. M. Fratila, J. M. de la Fuente, in *Nanomaterials for Magnetic and Optical Hyperthermia Applications* (Eds: R. M. Fratila, J. M. De La Fuente), Elsevier, Amsterdam **2019**, pp. 1–10.
- [20] J. Liu, H. Cui, S. Yan, X. Jing, D. Wang, L. Meng, *Mater. Today Commun.* **2018**, *16*, 97.
- [21] S. Lal, S. E. Clare, N. J. Halas, *Acc. Chem. Res.* **2008**, *41*, 1842.
- [22] I. Ortiz de Solorzano, T. Alejo, M. Abad, C. Bueno-Alejo, G. Mendoza, V. Andreu, S. Irueta, V. Sebastian, M. Arruebo, *J. Colloid Interface Sci.* **2019**, *533*, 171.
- [23] I. Ankareddi, M. M. Bailey, C. S. Brazel, J. F. Rasco, R. D. Hood, *Birth Defects Res., Part B* **2008**, *83*, 112.
- [24] H. S. Choi, Y. Ashitate, J. H. Lee, S. H. Kim, A. Matsui, N. Insin, M. G. Bawendi, M. Semmler-Behnke, J. V. Frangioni, A. Tsuda, *Nat. Biotechnol.* **2010**, *28*, 1300.
- [25] R. Monteagudo-Oliván, M. Arruebo, P. López-Ram-de-Viu, V. Sebastian, J. Coronas, *J. Mater. Chem. A* **2018**, *6*, 14352.
- [26] M. Sancho-Albero, B. Rubio-Ruiz, A. M. Pérez-López, V. Sebastián, P. Martín-Duque, M. Arruebo, J. Santamaría, A. Unciti-Broceta, *Nat. Catal.* **2019**, *2*, 864.
- [27] B. Rubio-Ruiz, A. M. Pérez-López, T. L. Bray, M. Lee, A. Serrels, M. Prieto, M. Arruebo, N. O. Carragher, V. Sebastián, A. Unciti-Broceta, *ACS Appl. Mater. Interfaces* **2018**, *10*, 3341.
- [28] S. Tang, M. Chen, N. Zheng, *Small* **2014**, *10*, 3139.
- [29] S.-W. Liu, L. Wang, M. Lin, Y. Liu, L.-N. Zhang, H. Zhang, *Chin. J. Polym. Sci.* **2019**, *37*, 115.
- [30] H. Kranz, N. Ubrich, P. Maincent, R. Bodmeier, *J. Pharm. Sci.* **2000**, *89*, 1558.
- [31] R. Chandan, A. Prabhakar, R. Banerjee, in *Stimuli Responsive Polymeric Nanocarriers for Drug Delivery Applications* (Eds: A. S. H. Makhoul, N. Y. Abu-Thabit), Woodhead Publishing, Cambridge **2019**, pp. 219–245.
- [32] a) A. Barhoumi, Q. Liu, D. S. Kohane, *J. Controlled Release* **2015**, *219*, 31; b) Y. Yang, J. Mu, B. Xing, *Wiley Interdiscip. Rev.: Nanomed. Nanobiotechnol.* **2017**, *9*, e1408.
- [33] R. Weissleder, *Nat. Biotechnol.* **2001**, *19*, 316.
- [34] S. Manna, Y. Wu, Y. Wang, B. Koo, L. Chen, P. Petrochenko, Y. Dong, S. Choi, D. Kozak, B. Oktem, X. Xu, J. Zheng, *J. Controlled Release* **2019**, *294*, 279.
- [35] a) H. Zhang, Y. Lu, G. Zhang, S. Gao, D. Sun, Y. Zhong, *Int. J. Pharm.* **2008**, *351*, 244; b) S.-N. Kim, B. H. Choi, H. K. Kim, Y. B. Choy, *J. Ind. Eng. Chem.* **2019**, *75*, 86.
- [36] a) X. Huang, S. Tang, X. Mu, Y. Dai, G. Chen, Z. Zhou, F. Ruan, Z. Yang, N. Zheng, *Nat. Nanotechnol.* **2011**, *6*, 28; b) V. Sebastian, C. D. Smith, K. F. Jensen, *Nanoscale* **2016**, *8*, 7534.
- [37] A. M. Alkilany, P. K. Nagaria, C. R. Hexel, T. J. Shaw, C. J. Murphy, M. D. Wyatt, *Small* **2009**, *5*, 701.
- [38] L. Herrero, V. Sebastian, S. Martín, A. González-Orive, F. Pérez-Murano, P. J. Low, J. L. Serrano, J. Santamaría, P. Cea, *Nanoscale* **2017**, *9*, 13281.
- [39] D. Zhang, C. Jin, H. Tian, Y. Xiong, H. Zhang, P. Qiao, J. Fan, Z. Zhang, Z. Y. Li, J. Li, *Nanoscale* **2017**, *9*, 6327.
- [40] D. Ding, Q. Zhu, *Mater. Sci. Eng., C* **2018**, *92*, 1041.
- [41] V. Andreu, A. Larrea, P. Rodriguez-Fernandez, S. Alfaro, B. Gracia, A. Lucía, L. Usón, A. C. Gomez, G. Mendoza, A. Lacoma, J. Dominguez, C. Prat, V. Sebastian, J. A. Ainsa, M. Arruebo, *Nanomedicine* **2019**, *14*, 707.
- [42] A. Patel, M. Patel, X. Yang, A. K. Mitra, *Protein Pept. Lett.* **2014**, *21*, 1102.
- [43] a) S. J. Pennycook, P. D. Nellist, Springer, New York **2011**; b) R. Arenal, K. March, C. P. Ewels, X. Rocquefelte, M. Kociak, A. Loiseau, O. Stephan, *Nano Lett.* **2014**, *14*, 5509.
- [44] I. Ortiz de Solorzano, G. Mendoza, M. Arruebo, V. Sebastian, *Colloids Surf., B* **2020**, *190*, 110904.
- [45] S.-Y. Li, M. Wang, *Mater. Lett.* **2013**, *92*, 350.
- [46] a) A. Bootz, V. Vogel, D. Schubert, J. Kreuter, *Eur. J. Pharm. Biopharm.* **2004**, *57*, 369; b) S. Bhattacharjee, *J. Controlled Release* **2016**, *235*, 337.
- [47] M. Jug, F. Maestrelli, M. Bragagni, P. Mura, *J. Pharm. Biomed.* **2010**, *52*, 9.
- [48] S. Streck, H. Neumann, H. M. Nielsen, T. Rades, A. McDowell, *Int. J. Pharm.: X* **2019**, *1*, 100030.
- [49] P. Ma, T. Li, H. Xing, S. Wang, Y. Sun, X. Sheng, K. Wang, *Biomed. Pharmacother.* **2017**, *89*, 689.
- [50] F. Tewes, E. Munnier, B. Antoon, L. Ngaboni Okassa, S. Cohen-Jonathan, H. Marchais, L. Douziech-Eyrolles, M. Soucé, P. Dubois, I. Chourpa, *Eur. J. Pharm. Biopharm.* **2007**, *66*, 488.
- [51] B. P. National Center for Biotechnology Information. "PubChem Compound Summary for CID 2474, <https://pubchem.ncbi.nlm.nih.gov/compound/Bupivacaine> (accessed: October 2020).
- [52] A. Setaro, M. Adeli, M. Glaeske, D. Przyrembel, T. Bisswanger, G. Gordeev, F. Mascietto, A. Faghani, B. Paulus, M. Weinelt, R. Arenal, R. Haag, S. Reich, *Nat. Commun.* **2017**, *8*.
- [53] B. P. Binks, J. H. Clint, *Langmuir* **2002**, *18*, 1270.
- [54] S. K. Ghosh, A. Boker, *Macromol. Chem. Phys.* **2019**, *220*, 1900196.
- [55] Q. Xu, M. Hashimoto, T. T. Dang, T. Hoare, D. S. Kohane, G. M. Whitesides, R. Langer, D. G. Anderson, *Small* **2009**, *5*, 1575.
- [56] W. D. Lindner, B. C. Lippold, *Pharm. Res.* **1995**, *12*, 1781.
- [57] N. Pettinelli, S. Rodríguez-Llamazares, Y. Farrag, R. Bouza, L. Barral, S. Feijoo-Bandín, F. Lago, *Int. J. Biol. Macromol.* **2020**, *146*, 110.
- [58] I. Permanadewi, A. C. Kumoro, D. H. Wardhani, N. Aryanti, *J. Phys.: Conf. Ser.* **2019**, *1295*, 012063.
- [59] F. Alexis, *Polym. Int.* **2005**, *54*, 36.
- [60] a) I. Mylonaki, E. Allémann, F. Delie, O. Jordan, *J. Controlled Release* **2018**, *286*, 231; b) G. Schliecker, C. Schmidt, S. Fuchs, R. Wombacher, T. Kissel, *Int. J. Pharm.* **2003**, *266*, 39.
- [61] N. Kamaly, B. Yameen, J. Wu, O. C. Farokhzad, *Chem. Rev.* **2016**, *116*, 2602.
- [62] N. Tan, K. Ji, D. He, S. Liao, L. He, J. Han, C. Chen, Y. Liu, *React. Funct. Polym.* **2020**, *147*, 104449.
- [63] ISO 10993–5:2009 [http://www.iso.org/iso/catalogue\\_detail.htm?csnumber=36406](http://www.iso.org/iso/catalogue_detail.htm?csnumber=36406) (accessed: October 2020).
- [64] C. G. Oliveira, L. F. Dalmolin, R. T. C. Silva, R. F. V. Lopez, P. I. S. Maia, J. A. Moreto, *New J. Chem.* **2020**, *44*, 14928.
- [65] M. A. Miller, B. Askevold, H. Mikula, R. H. Kohler, D. Pirovich, R. Weissleder, *Nat. Commun.* **2017**, *8*, 15906.
- [66] A. S. Nunes, A. S. Barros, E. C. Costa, A. F. Moreira, I. J. Correia, *Biotechnol. Bioeng.* **2019**, *116*, 206.
- [67] a) S. Breslin, L. O'Driscoll, *Drug Discovery Today* **2013**, *18*, 240; b) J. Lee, G. D. Lilly, R. C. Doty, P. Podsiadlo, N. A. Kotov, *Small* **2009**, *5*, 1213.
- [68] J. M. Lee, J. W. Choi, C. D. Ahrberg, H. W. Choi, J. H. Ha, S. G. Mun, S. J. Mo, B. G. Chung, *Microsyst. Nanoeng.* **2020**, *6*, 52.
- [69] L. F. Kou, Q. Yao, S. Sivaprakasam, Q. H. Luo, Y. H. Sun, Q. Fu, Z. G. He, J. Sun, V. Ganapathy, *Drug Delivery* **2017**, *24*, 1338.
- [70] a) Y. Gao, M. G. Li, B. Chen, Z. C. Shen, P. Guo, M. GuillaumeWientjes, J. L. S. Au, *AAPS J.* **2013**, *15*, 816; b) K. Y. Huang, H. L. Ma, J. Liu, S. D. Huo, A. Kumar, T. Wei, X. Zhang, S. B. Jin, Y. L. Gan, P. C. Wang, S. T. He, X. N. Zhang, X. J. Liang, *ACS Nano* **2012**, *6*, 4483.
- [71] a) H. Parshad, K. Frydenvang, T. Liljefors, C. Cornett, C. Larsen, *Eur. J. Pharm. Sci.* **2003**, *19*, 263; b) M. A. Paganelli, G. K. Popescu, *J. Neurosci.* **2015**, *35*, 831.